

Numerical analysis of the drag force of the flow in a square cylinder with a flat plate in front

M. Salinas-Vazquez, W. Vicente, E. Barrera, and E. Martinez
*Instituto de Ingenieria, Universidad Nacional Autonoma de Mexico,
 Ciudad Universitaria, 04510 Mexico D.F., Mexico.*

Received 2 October 2013; accepted 29 November 2013

Herein we present a numerical analysis of the drag force produced by the flow over a square cylinder with a flat plate positioned upstream thereof. The numerical model used to solve the compressible Navier-Stokes equations is based on a finite difference method, second order in time and fourth order in space. The plate height was varied from 20% to 100% the side of the square cylinder, and the distance between the plate and the cylinder was varied from 0.5 to 3.0 times the side of the cylinder. The Reynolds number was considered to be 650, based upon the side of the cylinder and the inflow speed. The numerical predictions show that, for some cases, the total drag force produced by the square cylinder and plate system is lower than that of the square cylinder only.

Keywords: Wake; square cylinder; aerodynamics; large eddy simulation.

PACS: 47.21.-i; 47.27.Gs; 47.40.Dc

1. Introduction

The forces acting on bodies immersed in a fluid have been subject of interest in recent decades. Some applications, where aerodynamic drag reduction is directly related, are the design of bridges and buildings, optimization in heat exchangers and turbo-machinery components.

Some of the first studies were from Morel & Bohn [1], Igarashi & Terachi [2], and Koenig & Roshko [3]. In this works, two bodies were placed in series. The results showed that in some cases, the total drag was reduced in contrast with the drag acting only over one of the bodies. The importance of acoustic effects, responsible of vibrations in the configuration [4], was acknowledged in subsequent experimental investigations. This problem has led to the use of the more sophisticated instrumentation available for its study, which is still a matter of discussion if the large scales are responsible for the predominant energy in fluctuations. In fact, the modern implementation of non-intrusive experimental techniques such as Laser Doppler [4] and particle image velocimetry [5] have been efforts to get more accurate results of acoustics and aerodynamics.

Numerical analysis in two dimensions ([6] and [7]) and three dimensions [8] have successfully reproduced the phenomenon for laminar flow and low Reynolds numbers. However, in spite of technological advances, Direct Numerical Simulation remains as a high computational cost alternative limited to low Reynolds numbers and simple geometries. Consequently, a Large Eddy Simulation (LES) has been implemented in the present work in order to analyze the drag force produced by the flow around a square cylinder when a flat plate is positioned upstream thereof. The main advantage of performing a LES is that the fine details of the turbulence are obtained for the studied Reynolds numbers.

The plate height is varied from 0.2 to 1.0 times the width of the square cylinder, and for each height, the perpendicu-

lar distance between the control plate and the cylinder ranged from 0.5 to 3.0 times the width of the cylinder. The Reynolds number was considered to be 650, based upon the width of the cylinder and the inflow speed. The drag force acting on both the cylinder and the complete configuration (square cylinder - plate) is also presented herein.

2. Mathematical model

The governing equations for a compressible flow, considering it as an ideal gas, are the conservation of mass and energy as well as the momentum equation; in a Cartesian frame of reference, they can be written as:

$$\frac{\partial \mathbf{U}}{\partial t} + \frac{\partial \mathbf{F}_i}{\partial x_i} = \mathbf{S} \quad (1)$$

where \mathbf{U} is a five-component vector defined by:

$$\mathbf{U} = (\rho, \rho u_1, \rho u_2, \rho u_3, \rho e)^T \quad (2)$$

Moreover, it is considered that $\mathbf{u} = (u_1, u_2, u_3)$ is the velocity vector and, ρ is the density. The velocity vector is also written as $\mathbf{u} = (u, v, w)$. Equation (1) represents the evolution of density (continuity equation), momentum and total energy defined for an ideal gas as follows:

$$\rho e = \rho C_\nu T + \frac{1}{2} \rho (u_1^2 + u_2^2 + u_3^2) \quad (3)$$

In Eq. (1), \mathbf{F}_i are fluxes in the three directions, where $\forall i \in \{1, 2, 3\}$, and for a Newtonian fluid, are given by:

$$\mathbf{F}_i = \begin{pmatrix} \rho u_i \\ \rho u_i u_1 + p \delta_{i1} - 2\mu S_{i1} \\ \rho u_i u_2 + p \delta_{i2} - 2\mu S_{i2} \\ \rho u_i u_3 + p \delta_{i3} - 2\mu S_{i3} \\ (\rho e + p) u_i - 2\mu u_j S_{ij} - k \frac{\partial T}{\partial x_i} \end{pmatrix} \quad (4)$$

where $k = \rho C_p \kappa$ is the thermal conductivity and κ the thermal diffusivity. The symbol δ_{ij} is the Kronecker's delta and δ_{ij} is the deviatoric component of the deformation tensor. The term S_{ij} can be written as:

$$S_{ij} = \frac{1}{2} \left(\frac{\partial u_i}{\partial x_j} + \frac{\partial u_j}{\partial x_i} - \frac{2}{3} (\nabla \cdot u) \delta_{ij} \right) \quad (5)$$

The molecular viscosity is established through the empirical Sutherland's law [9]:

$$\mu(T) = \mu(T_{ref}) \left(\frac{T}{T_{ref}} \right)^{\frac{1}{2}} \frac{1 + \frac{S}{T_{ref}}}{1 + \frac{S}{T}} \quad (6)$$

where S , T_{ref} and $\mu(T_{ref})$ are properties of the gas. The thermal conductivity $k(T)$ is obtained assuming molecular Prandtl number is:

$$Pr = \frac{\nu}{\kappa} = \frac{C_p \mu(T)}{k(T)} \quad (7)$$

For this analysis, the Prandtl number is considered to be 0.7 (air). The classical equation of state regarding the static pressure p , temperature T , and density ρ is:

$$p = R\rho T \quad (8)$$

and closes the system of equations, with $R = C_p - C_v$. $\gamma = C_p/C_v$, which is constant and equal to 1.4. C_p and C_v are the specific heat capacity at constant pressure and volume respectively [10].

For turbulent flows, the system of equations is closed with the Large Eddy Simulation technique, which consists of directly simulate large flow scales, that is, scales that are larger than the local grid size, whereas small scales, or those smaller than the local grid size are filtered, and their effect on large scale movement is modeled based on a subgrid model. The model that was used in this work is the selective structure function model, which is an extrapolation to the physical space of the spectral model [11-13].

The system in generalized coordinates is solved by means of an extension of the explicit McCormack scheme, second order in time and fourth order time in space, developed by Gottlieb & Turkel [14]. This numerical scheme is a corrector - predictor scheme using generalized coordinates. The adaptation to the generalized coordinates (allowing the use of a non-uniform grid) is performed by introducing a Jacobian matrix, which transforms a non-uniform grid complex geometry or curvilinear geometry, into a Cartesian coordinate system within a simple orthogonal geometry with a uniform grid in the generalized coordinate system (ξ_1, ξ_2, ξ_3) [9].

Due to the use of the Large-Eddy Simulation, the temporal discretization requires to be explicit (as much as possible in order to avoid numerical diffusion), which entails significant restrictions on the value of the time step. To prevent small time steps, as a result of the correct acoustic simulation of the problem, we used an alternative method [15] to that developed by Wang & Trouvé [16]. This method consists of only adding the acoustic part of the expansion to the energy

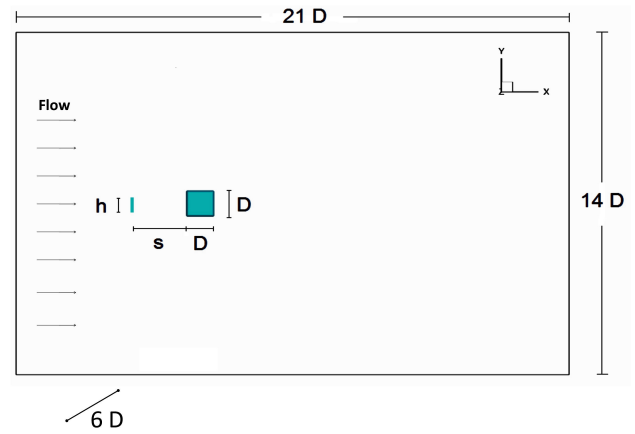


FIGURE 1. Scheme of the configuration to be simulated.

equation. This simple procedure can rescale the speed of sound into similar values to that of the flow velocity under analysis.

Finally, both the cylinder and the plate were created from the immersed boundaries method [17]. The boundary conditions are based on the resolution of the local wave equations on the boundary [18].

3. Description of the problem

The system to be simulated consists of a square cylinder of infinite length positioned in a channel, as shown in Fig. 1. The width of the square, D , is taken as the reference length. The cylinder is placed in the center of the vertical distance ($7D$) and at a distance of $6.5D$ from the input of the computational domain. In the direction of length of the cylinder, the distance of the simulated domain is $6D$, and periodic conditions are placed at the ends to simulate an infinite length. A plate of variable height h and with negligible thickness is placed upstream of the square cylinder. The distance between the cylinder and the plate is, s . The inlet and outlet boundaries are the left and right edges in Fig. 1, respectively. The thermodynamic variables of the inflow (P_0 and T_0), inlet speed (U_0) and viscosity (ν_0), are considered as reference values, atmospheric conditions. The Reynolds number based on these reference values is $Re = 650$.

4. Numerical details

The simulations are brought into a three-dimensional domain $21D \times 14D \times 6D$ in x , y and z directions, respectively. The computational domain has $180 \times 139 \times 80$ nodes in the x , y and z directions, respectively. The grid has been refined in those areas where the greatest shear stresses are expected, which is shown in Fig. 2. Both the dimensions and the resolution of the calculation domain were obtained from a grid independence study [19]. The boundary conditions are based on the work of Poinso & Lele [18]. The inlet and outlet of

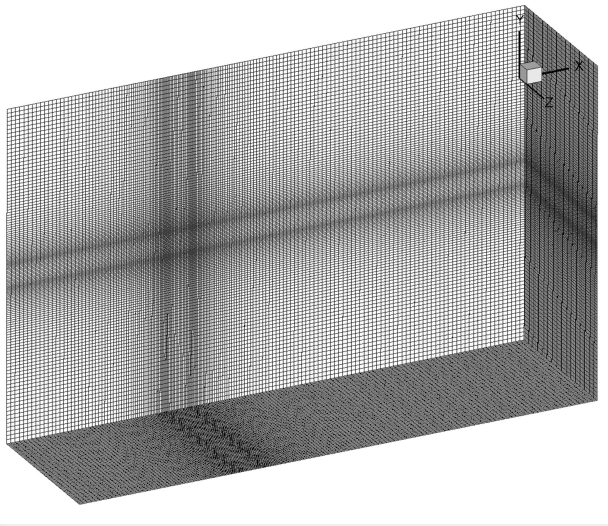


FIGURE 2. Grid of the computational domain used in the simulations.

the flow ($i = 1$ and $i = nx$, respectively) is a subsonic input and non-reflecting subsonic output. Slip conditions at the walls were imposed in the y direction, and finally periodic boundary conditions were imposed in the z direction, which are used to simulate the infinite length of the cylinder, see Fig. 2. As initial condition, the three velocity components are null and the thermodynamic variables, pressure and temperature, have their reference values (atmospheric values).

The mean values of the variables are obtained by averaging the instantaneous signal in time and in the homogeneous z direction (direction of the length of the cylinder).

5. Results

Several simulations were performed where the distance s , and the plate height, h , of the control plate (see Fig. 1), were changed in order to know the effect of these modifications in the flow behavior. Table I provides the nomenclature used for the presentation of the results of each of the studied cases. It is noteworthy that only the cases represented with a letter are presented in this paper. However, all 21 possible cases shown in the table were performed. Case A is the base case where the control plate is not used. The shaded cells shown in Table I correspond to the same case A, when $s/D=0$ and/or $h/D=0$.

5.1. Numerical validation

Both the code and the flow configuration were validated from the comparison with experimental data on parameters such as the lift, drag and pressure coefficients, and the Strouhal number [19]. In this paper, we performed numerical simulations of the flow around a rectangular cylinder (without control plate) for different Reynolds numbers.

For the case of this work, $Re=650$, the half drag coefficient value, C_d , predicted by the numerical model for the

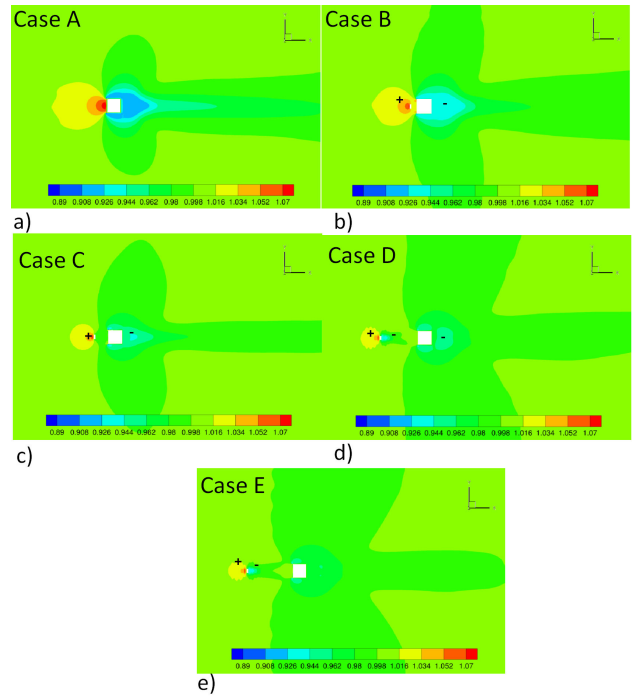


FIGURE 3. Mean pressure fields in an x - y plane, for cases A (a), B (b), C (c), D (d) and E (e). Dimensionless pressure values, P/P_o .

cylinder without the control plate (Case A) is 2.088; experimentally, it was found ranging from $C_d \approx 2.05$ to 2.1. For this same case, the Strouhal number calculated by the model is $St=0.1732$; experimentally, it was found to range from $St \approx 0.12$ to 0.16 [20]. Finally, it was found that the predicted mean lift coefficient was $C_l \approx 0$.

6. Pressure fields

Mean pressure fields for cases A, B, C, D and E are shown in Fig. 3. The zones with higher pressure occur when the flow hits the control plate, stagnation zone, while low-pressure areas are associated with regions of high flow velocity, but above all, with recirculation zones mainly formed behind both bodies. In cases A and B, these recirculation zones appear only behind the cylinder. However, recirculations also appear in the area separating both bodies for cases C, D and E, being more evident in cases D and E. This was due, mainly, to the boundary layer separation and the creation of vortices behind both bodies

As may be confirmed by subsequent analysis, drag reduction is closely related to the difference between the pressures upstream and downstream of the bodies under study. The drag is directly proportional to this pressure difference for this configuration. For aerodynamic geometries, *i.e.* circular section, the drag is also strongly dependent on the shear stress over the wall of the body.

Figure 4 shows the average pressure contours for cases F, G, H, and I. As the control plate grows in its height, the decreasing of pressure is accentuated behind it as well as an increase in the size of the high pressure zone upstream thereof.

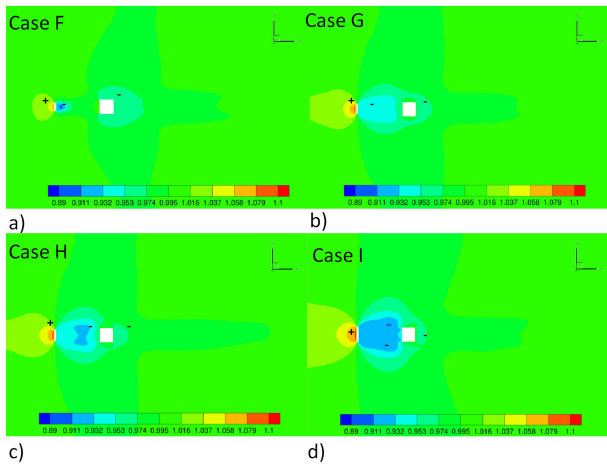


FIGURE 4. Mean pressure fields in an x-y plane, for cases F (a), G (b), H (c) and I (d). Dimensionless pressure values, P/P_0 .

The pressures before and after the cylinder are balanced; thus, decreasing the drag force on it. As it will be seen later, the drag force values on the cylinder will become negative in the cases H and I.

A simple way is to visualize the turbulent structures is by displaying iso-surfaces of the criterion Q [21] (second invariant of the velocity gradient). $Q=1/2 (\Omega_{i,j}\Omega_{i,j} - S_{i,j}S_{i,j})$, where $\Omega_{i,j}$ is the antisymmetric part and $S_{i,j}$ is the symmetric part of the velocity gradient. Figure 5 shows the iso-surfaces for a dimensionless value $Q = 200$ for the different studied cases. Three points are characterized in the figures. Point 1 identifies the boundary layer separation, where the flow has its maximum acceleration. Point 2 identifies antisymmetric large vortices formation behind the bodies (Von Karman Street). The axis of rotation of these structures is perpendicular to the free stream flow. Finally, point 3 identifies the moment at which the turbulence becomes three-dimensional. The larger structures identified in point 2 begin to deform in an S-shape, leading to structures in which longitudinal vorticity is intensified.

In these figures, it can also be observed that the flow from the free stream hits the control plate, generating vortex shedding from their ends and entraining irrotational flow from the free stream, creating a small recirculation zone between the bodies (plate and cylinder). Later on, the flow sticks to the horizontal faces of the cylinder. The flow in this region will depend on the values of both h and s .

In particular, when the distance between the bodies is not very large, for example, cases B and C, two quasi-stationary vortices are formed between the two bodies (which remain in this position throughout the study, with only small oscillations), joining both bodies like a more aerodynamic body. In the case C, the size of the vortices is larger because the distance s was also increased, which is why there is a better coupling towards the horizontal faces of the cylinder. For the same case C, it is observed that the width of the wake behind the cylinder is qualitatively smaller compared with the other cases. In this instance, the control plate achieves its better reduction effect of the overall drag of both bodies.

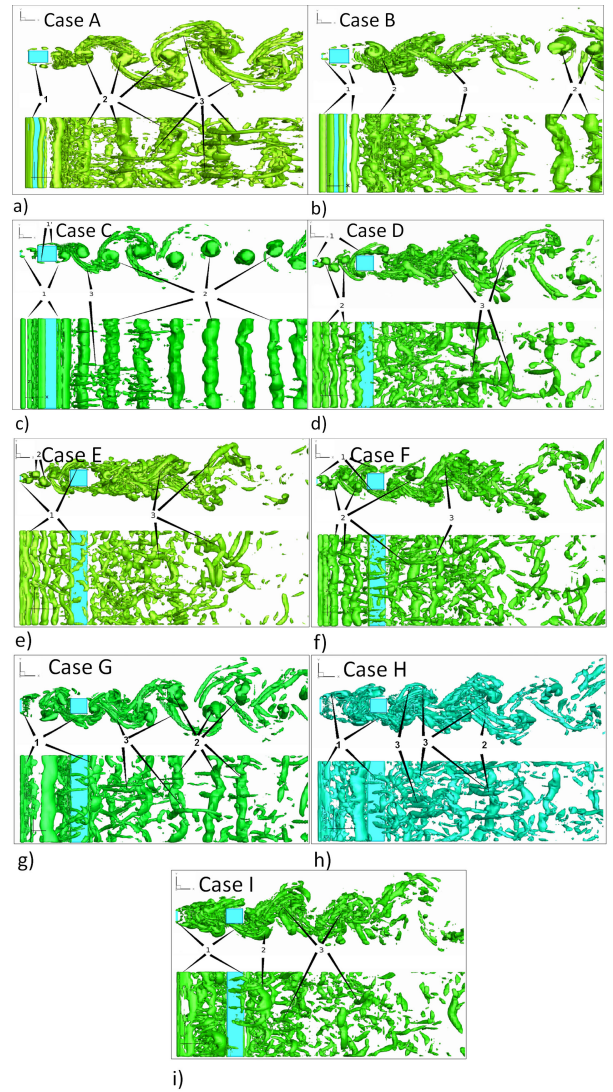


FIGURE 5. Topology of the turbulent structures in the studied configurations. Cases A (a), B (b), C (c), D (d), E (e), F (f), G (g), H (h), and I (i). Isosurfaces of criterion Q , ($Q/(U_0/D)=200$).

The cases D and E show that the distance between the bodies is large enough so that the Von Karman Street develops behind the plate, vortices somewhat two-dimensional. In the case E, the flow takes place afterwards, reaching a completely turbulent character. For the case F, the turbulence is fully developed (three-dimensional) and the cylinder is immersed in it.

In cases G, H and I, where the plate height, h , is large, the occurrence of the Von Karman Street becomes again perceived behind the cylinder, which is evidenced by the appearance of longitudinal vortices immediately downstream the cylinder and its fast development in a three-dimensional turbulence. However, the flow behind the plate is likewise a fully developed turbulence. Such cases can be interesting in particular if the heat transfer between the cylinder and the flow is to be increased.

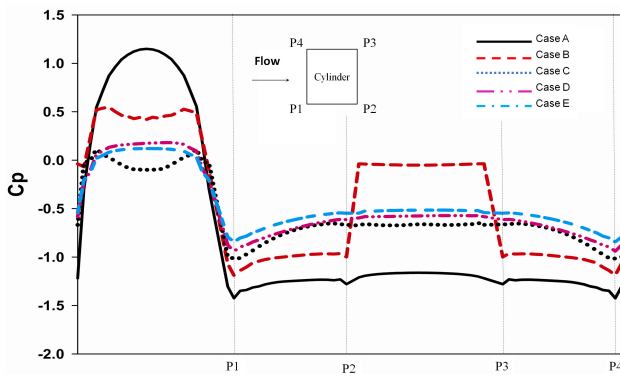


FIGURE 6. Pressure coefficient on the surface of the cylinder. Cases A, B, C, D and E.

7. Aerodynamic coefficients

Figure 6 shows the mean pressure coefficient distribution ($C_p = (P - P_0)/(1/2\rho U_0^2)$) over the entire surface of the cylinder for different cases (Cases A, B, C, D and E). The solid line denotes the pressure coefficient obtained when the plate is not present in the configuration, for instance, case A. The remaining lines correspond to the pressure coefficient on the cylinder when the plate is placed in front of it. When the control plate is used, the pressure coefficient is lower than in case A for the front face (P1-P4). On this front side, in cases B and C, the pressure distribution is concave, while for D and E cases the distribution is convex, because the stagnation zone is located mainly in the front face of the plate and cylinder edges (points P1 and P4). On the rear face (points P2-P3), the pressure decreases, even for case B, wherein there is an increment compared to the other cases. Similar results in the pressure distribution were found in similar experimental work to the preset simulated case but for higher Reynolds number [22], and for a flow around two square cylinders [5].

Figure 7a shows the ratio between the drag coefficient $Cd(C_d = F_d/(1/2\rho AU_0^2))$, where A is the surface of the plate and / or cylinder, and the location of the control plate with respect to the cylinder, s , and its height h . The drag coefficient was obtained by integrating the pressure and the wall shear stress on all faces of both bodies. It is noted that the drag acting on the cylinder decreases in all cases when the plate is placed in front of it, which produces a low pressure area due to the formation of the wake behind the plate.

From Fig. 7, it can be seen that there is proportionality between the height of the plate and the reduction of the drag coefficient on the cylinder. As shown in Fig. 5, in cases E, F and G, vortices are created on an alternating basis behind the plate wake, while in cases H and I, the turbulence is practically three-dimensional. This causes the pressure in the front face of the cylinder to become smaller as the plate height increases. For this configuration, the drag force is mainly related to the distribution of pressures on the surface of the bodies. When the plate is large enough, cases $h/D = 0.8$ and 1.0 , the drag coefficient on the cylinder is negative. This change

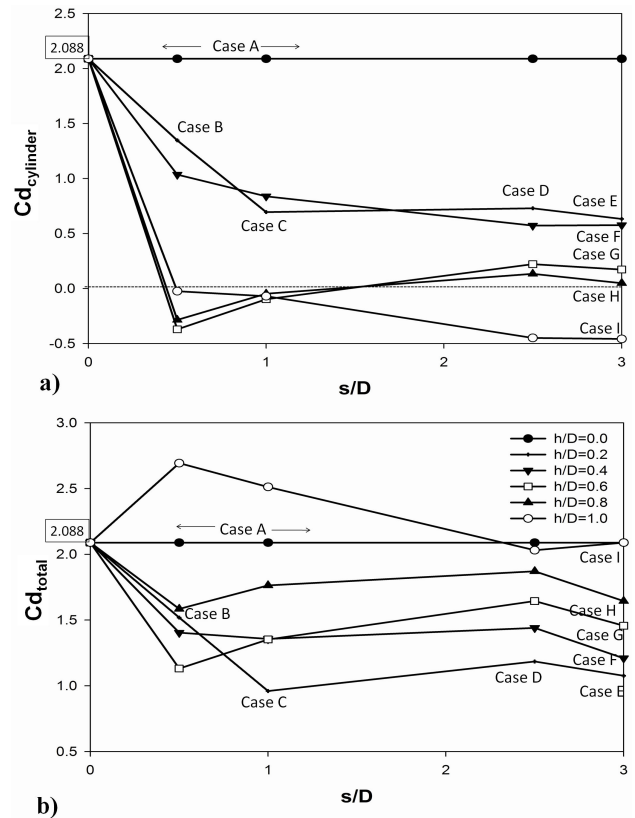


FIGURE 7. Drag coefficient variation with distance of separation s/D for different heights h/D (21 cases of Table I). a) Only in the cylinder, b) The sum in both bodies, cylinder and plate.

indicates that the horizontal force acting on the cylinder has changed its direction; thus, it becomes a force that pushes the cylinder in opposite direction to the flow direction.

Figure 7b shows the total drag coefficient in the system, which is the sum of the coefficient acting on the cylinder and the plate. This coefficient is shown as a function of the plate position for different heights. Figure 7b shows that the total drag coefficient increases as the plate height increases. The most significant case of such behavior is when $h/D = 1.0$, where the total drag becomes even greater than that obtained in the configuration without plate, case A. For case I, despite having the greatest total drag coefficient (of the cases studied in this paper), the lowest coefficient was only found in the cylinder. The case C has the lowest total drag coefficient; less than 50% of that obtained for the case A. According to Fig. 5, case C is the one with a higher dimensional behavior in the turbulent structures, indicating that the flow is in transition without a marked development of the turbulence.

For the cases previously analyzed, three different flow configurations can generally be seen, as shown schematically in Fig. 8. The first configuration corresponds to the highest reduction of the drag coefficient in both bodies, case C; two quasi-stationary symmetric vortices are formed between the bodies. This allows coupling of the two bodies into one with a more aerodynamic geometry. The second configuration occurs in case E; a greater separation between the bodies gives

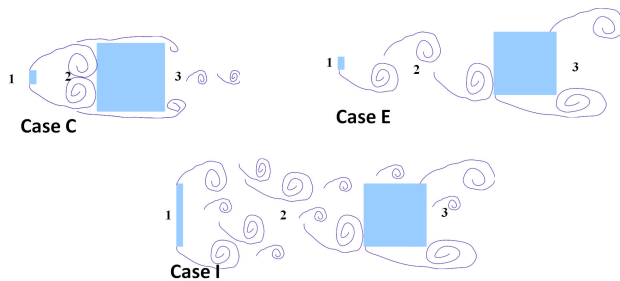


FIGURE 8. Schematic configuration of the flow for the most representative cases: C, E and I (Table I).

rise to antisymmetric vortices (Von Karman Street), which affect the coupling between both bodies, decreasing the pressure difference between the faces upstream and downstream of the cylinder (between points 2 and 3, Fig. 8), but increasing it between the faces of the plate (between points 1 and 2, Fig. 8). Finally, the third configuration corresponds to case I; the turbulence in the wake behind the plate is completely developed, leaving the cylinder within this turbulent flow. In recent cases (G, H, and I) substantial increases of the total drag coefficient are present, but negative values of this coefficient are obtained if it is only calculated in the cylinder. These configurations were also observed by Igarashi & Terachi [2] and Igarashi [23].

8. Conclusions

In this paper, numerical simulations of the flow with the Large Eddy Simulation approach were performed to study the influence of a flat plate in the drag force produced by the flow over a square cylinder of infinite length. The model uses an immersed boundaries technique which allows the use of high order schemes.

To validate the model, we compared the case where only the square cylinder is exposed to the flow, with experimental data obtained by other authors. The results obtained in this

study show a good approximation to the corresponding experimental results. The flow analysis was done by varying the size and position of the plate, which was placed upstream of the cylinder.

From the results presented herein, we conclude that those configurations where a reduced total drag is present correspond to those where the bodies are coupled to form a more aerodynamic profile. Case C is the most representative case where the turbulence in this flow is not fully developed; thus staying in transition (quasi-bidimensional structures) in the entire configuration. In contrast, due to the poor development of the turbulence, poor mixing conditions in such cases were observed, which may be an undesirable characteristic in some applications such as heat transfer. This work provides the basis for heat transfer problems and/or combustion, where the challenge will be to find a balance between aerodynamic forces and heat transfer.

On the other hand, there were cases where the drag on the cylinder was negative; the effect of the plate height determined the presence of these cases. However, for these cases the total drag was increased when compared with the case without plate, which can lead to unwanted effects mainly on aerodynamic and structural applications. In these cases, the flow characteristics were a three-dimensional turbulence fully developed downstream of both bodies; in some cases, higher turbulent interaction in space between the bodies and downstream of the cylinder can happen.

Acknowledgements

This work was developed in the cluster Tonatiuh of the Instituto de Ingenieria, UNAM. The authors gratefully acknowledge Fernando Maldonado, cluster manager, and his team ASUL for all the facilities and support. On the other hand, we appreciate the support given to the research presented here by Universidad Nacional Autonoma de Mexico, PAPIIT DGAPA- IN106112.

1. T. Morel, and M. Bohn, *ASME Journal of Fluids Engineering* **102** (1980) 104.
2. T. Igarashi and N. Terachi, *Journal of Wind Engineering and Industrial Aerodynamics*, **90** (2002) 359.
3. K. Koenig, and A. Roshko, *Journal of Fluid Mechanics* **156** (1985) 167.
4. A. Mohany, and S. Ziada, *Journal of Fluids and Structures* **25** (2009) 461.
5. Md. Mahbub Alam, and Y. Zhou, *Journal of Fluids and Structures* **24** (2008) 505.
6. A. Mussa, P. Asinari and L.S Luo. *Journal of Computational Physics* **228** (2009) 983.
7. P.F. Zhang, J.J. Wang, and L.X. Huang, *Applied Ocean Research* **28** (2006) 183.
8. J. Deng, A.L. Ren, J.F. Zou, and X.M. Shao, *Fluid Dynamics Research* **38** (2006) 386.
9. C. A. Fletcher, *Computational techniques for fluid dynamics 2*. (Springer-Verlag 1988).
10. M. Salinas-Vazquez, and O. Métais, *Journal of Fluid Mechanics* **453** (2002) 201.
11. M. Lesieur, and O. Métais *Annual Review of Fluid Mechanics* **28** (1996) 45.
12. M. Lesieur, and P. Comte, *Large eddy simulations of compressible turbulent flows. Dans Turbulence in Compressible Flows*, (AGARD/VKI Course, AGARD report 819 1997).
13. E. David Modélisation des écoulements compressibles et hypersoniques: Une approche instationnaire. PhD Thesis, (Institut National Polytechnique de Grenoble, France 1993).

14. D. Gottlieb and E. Turkel *Mathematics of Computation* **30** (1976) 703.
15. M. Salinas-Vazquez, W. Vicente, E. Martinez, and E. Barrios, *International Journal of Heat and Fluid Flow* **32** (2011) 876.
16. Y. Wang and A. Trouvè, *Combustion, Theory and Modelling* **8** (2004) 633.
17. M. Salinas-Vazquez, M.A. de la Lama, W. Vicente, and E. Martinez, *Applied Mathematical Modelling* **35** (2011) 4393.
18. T.J. Poinsot, and S.K. Lele, *J. Computational Physics* **101** (1992) 104.
19. M. Salinas-Vazquez, E. Chol-Orea, V. Leyva-Garcia, and W. Vicente-Rodríguez, *Rev. Mex. Fis.* **53** (2007) 461.
20. A. Sohankar, C. Norberg, and L. Davidson, *Phys. Fluids* **11** (1999) 288.
21. J.C.R. Hunt, A.A. Wray, and M.P. Eddies, *Center for turbulence Research Report CTR-S88*, (1988) pp. 193.
22. H. Sakamoto, K. Tan, N. Takeuchi, and H. Haniu *Journal of Fluids Engineering* **119** (1997) 506.
23. T. Igarashi, *Bulletin of the JSME* **25** (1982) 349.